magnetochemistry

MDPI

Article

Magnetic and Magnetocaloric Properties of $ErFe_3(BO_3)_4$: The Role of the Crystallographic Environment

Assaad Elouafi [1,2,*], Piotr Gębara [3], Z. Fadil [4], M. Naziruddin Khan [5], Abdulrahman A. Alsayyari [6] and Chaitany Jayprakash Raorane [7,*]

1 Laboratory of Processes, Mechanics, Materials, and Industrial Engineering, Higher School of Technology, Hassan II University de Casablanca, Casablanca B.P. 8012, Morocco
2 Interdisciplinary Laboratory of Fundamental and Applied Sciences, Higher Normal School, Hassan II University de Casablanca, Casablanca B.P. 8012, Morocco
3 Department of Physics, Częstochowa University of Technology, Armii Krajowej 19, 42-200 Czestochowa, Poland
4 Laboratoire de Matière Condensée et Sciences Interdisciplinaires (LaMCScI), URL-CNRST, Faculty of Sciences, Mohammed V University in Rabat, Rabat B.P. 1014, Morocco
5 Department of Physics, Faculty of Science, Islamic University of Madinah, Madinah 42351, Saudi Arabia; mnkhan_phy@yahoo.com
6 Department of Radiologic Technology, College of Applied Medical Sciences, Qassim University, Buraydah 51452, Saudi Arabia
7 School of Chemical Engineering, Yeungnam University, Gyeongsan 38541, Republic of Korea
* Correspondence: assaadelouafi@gmail.com (A.E.); chaitanyaraorane22@ynu.ac.kr (C.J.R.)

Abstract

The interplay between crystallographic symmetry, the local rare-earth environment, and magnetic interactions provides a useful framework for understanding the low-temperature magnetic and magnetocaloric properties of rare-earth-containing compounds. In this study, the structural, magnetic, and magnetocaloric properties of polycrystalline $ErFe_3(BO_3)_4$ are investigated. Room-temperature X-ray diffraction analysis confirms the formation of a trigonal phase described by the non-centrosymmetric space group R32 (No. 155), characteristic of the huntite-type structure. Magnetic measurements reveal a magnetic transition at approximately 38 K. The magnetocaloric effect is evaluated from the field-dependent magnetization using the Maxwell relation. The maximum magnetic entropy change reaches approximately 9.0 J kg^{-1} K^{-1} for a magnetic-field change of 0–7 T. The temperature-averaged entropy change over a selected 5 K interval is approximately 8.20 J kg^{-1} K^{-1}, while the relative cooling power (RCP) is approximately 235 J kg^{-1}. These results are discussed in terms of the possible contributions of the local Er^{3+} environment, crystal-field effects, magnetic anisotropy, and interactions between the Er^{3+} and Fe^{3+} magnetic subsystems. The findings establish the magnetocaloric response of $ErFe_3(BO_3)_4$ and provide a basis for further investigation of the interplay between its crystallographic environment and magnetic interactions.

Keywords: $ErFe_3(BO_3)_4$; rare-earth ferroborate; crystallographic symmetry; magnetic anisotropy; crystal-field effects; antiferromagnetic ordering; magnetocaloric effect; magnetic entropy change; relative cooling power

Academic Editors: Peijiang Liu, Jianping Peng and Xiaodong Jian

Received: 26 October 2026
Revised: 10 November 2026
Accepted: 12 November 2026
Published: 16 November 2026

Copyright: © 2026 by the authors. Licensee MDPI, Basel, Switzerland. This article is an open access article distributed under the terms and conditions of the Creative Commons Attribution (CC BY) license.

1. Introduction

The development of efficient solid-state refrigeration technologies has stimulated increasing interest in magnetic materials exhibiting significant and reversible magnetocaloric effects (MCEs), particularly in the cryogenic temperature range [1–4]. The magnetocaloric effect originates from the coupling between an applied magnetic field and the magnetic degrees of freedom of a material, leading to a field-induced variation in magnetic entropy and, under adiabatic conditions, a change in temperature. The magnetocaloric performance is commonly evaluated in terms of the magnetic entropy change ΔS_M, the adiabatic temperature change ΔT_{ad}, and the relative cooling power (RCP) [1–4]. In recent years, particular attention has been devoted to rare-earth-based compounds because their localized 4f electrons provide large magnetic moments and a rich variety of magnetic ground states, resulting in diverse low-temperature magnetic and magnetocaloric behaviors [2–6].

The magnetic properties of rare-earth compounds are governed by exchange interactions, spin–orbit coupling, crystal-field effects, and magnetic anisotropy [5–9]. In particular, the local crystallographic environment surrounding a rare-earth ion determines the crystal-field potential and consequently the splitting of its 4f electronic states. This splitting controls the occupation of low-energy magnetic states and can substantially modify the magnetic anisotropy and field-dependent magnetization. Recent studies have demonstrated that crystal-field effects and magnetic anisotropy can have a decisive influence on the magnetocaloric response of rare-earth materials [6–11]. Large anisotropic magnetocaloric effects have, for example, been reported in rare-earth single crystals, where the orientation of the applied magnetic field relative to the crystallographic axes strongly modifies the magnetic entropy change [7–11]. These observations emphasize that the magnetocaloric response should be considered not only in terms of the magnetic transition temperature but also in relation to the microscopic electronic and structural environment of the magnetic ions.

From a crystallographic perspective, symmetry provides a fundamental framework for understanding the relationship between the local electronic environment and magnetic properties. A change in crystallographic symmetry can modify atomic positions, coordination geometries, bond lengths, bond angles, and exchange pathways, thereby affecting magnetic interactions and anisotropy [12–14]. This relationship is particularly important in compounds containing rare-earth ions, for which relatively small modifications of the local coordination environment can produce significant changes in the crystal-field scheme. Recent investigations have demonstrated that modifications of the rare-earth–oxygen environment can alter crystal-field levels and magnetic anisotropy, with important consequences for low-temperature magnetic and magnetocaloric properties [9,10]. Symmetry analysis has therefore become an increasingly useful approach for describing structural distortions, magnetic states, and symmetry-dependent physical properties in complex magnetic materials [12–14].

Rare-earth iron borates, $RFe_3(BO_3)_4$, constitute an interesting family of materials for investigating the interplay between crystal structure and magnetic properties. Their physical behavior is governed by the combined contributions of the Fe^{3+} and rare-earth magnetic sublattices, including exchange interactions, crystal-field effects, and magnetic anisotropy. These interactions can give rise to complex magnetic, magnetoelectric, and magnetoelastic phenomena, making this family particularly relevant for exploring the relationship between magnetic ordering and magnetocaloric properties [15–18].

Recent studies have highlighted the role of magnetic anisotropy and spin–lattice interactions in magnetocaloric materials. An anisotropic magnetocaloric effect and spin–phonon coupling have been reported in $FePS_3$, highlighting the influence of magnetic ordering and lattice dynamics on its thermodynamic properties [19]. Further

https://doi.org/10.3390/magnetochemistry12110129

investigations have reported magnetocaloric properties and magnetic phase transitions in several rare-earth compounds, including $YbVO_3$, NdNi, $DyMn_2Ge_2$, and $Er_{1-x}Tm_xAl_2$ [20–24]. In $ErFe_3(BO_3)_4$, pressure-induced structural transitions, magnetic ordering, and the influence of the local environment of Er^{3+} ions have also been investigated [22,25–27]. Significant magnetocaloric effects have been reported in rare-earth borates, such as Gd_3TeBO_9, $Eu_2B_2O_5$, and $Ba_5Gd_3(BO_3)_6F$ [28–30]. Anisotropic magnetocaloric behavior has also been observed in $DyTe_3$ and NdGaSi single crystals [31,32], while further studies have explored magnetic refrigeration in $Sr_{14.06}Gd_{14.63}(BO_3)_{24}$ and other rare-earth borates [33–35].

In particular, the magnetic state of the rare-earth subsystem is strongly influenced by the exchange field generated by the Fe^{3+} ions, while the rare-earth crystal-field states can, in turn, influence the magnetic anisotropy and low-temperature magnetic behavior.

$ErFe_3(BO_3)_4$ is particularly interesting within this family because the Er^{3+} ion possesses a strongly anisotropic 4f electronic configuration that is highly sensitive to its local crystallographic environment. At high temperatures, $ErFe_3(BO_3)_4$ crystallizes in the trigonal R32 space group (No. 155), whereas cooling induces a structural transition to the lower-symmetry $P3_121$ phase, as reported in previous studies [22].

Structural investigations of rare-earth iron borates have shown that symmetry changes can be accompanied by modifications in atomic positions, coordination-polyhedron distortions, and Fe–O–Fe exchange and superexchange pathways [13]. For $ErFe_3(BO_3)_4$ specifically, recent pressure-dependent studies have demonstrated that the crystal structure and the local Er^{3+} environment are sensitive to external pressure, with structural transitions involving $P3_121$, $P3_21$, and R32 symmetries [22].

Detailed structural investigations of rare-earth iron borates have shown that this symmetry reduction is accompanied by modifications of interatomic distances, coordination-polyhedron distortions, and Fe–O–Fe exchange and super-exchange pathways [13]. More recently, pressure-dependent investigations of $ErFe_3(BO_3)_4$ have demonstrated that its crystal structure is highly sensitive to external pressure, with a sequence of structural phase transitions involving $P3_121$, $P3_221$, and R32 symmetries [22]. The pressure study further showed that the local symmetry of Er^{3+} and the crystal-field environment evolve with the structural state, providing direct evidence for the strong relationship between crystallographic symmetry and the rare-earth electronic degrees of freedom [22]. These findings establish a structural basis for examining how the local Er^{3+} environment may be relevant to the magnetic and magnetocaloric properties of this compound.

The local environment of Er^{3+} is particularly relevant because its 4f electronic states are highly sensitive to crystal-field effects. In the low-temperature P31 21 phase, the local symmetry of the Er^{3+} site is reduced compared with that in the high-temperature R32 structure [13,19]. Optical and magneto-optical investigations have provided direct evidence of this sensitivity. Malakhovskii et al. demonstrated substantial differences in the absorption and magnetic circular dichroism spectra of $ErFe_3(BO_3)_4$ associated with the low local symmetry of Er^{3+} [26]. Their results showed that relatively small local distortions can strongly affect the splitting and character of the 4f–4f transitions. In particular, the local symmetry reduction was found to produce distinct spectroscopic features that were absent or much weaker in the higher-symmetry reference compound $ErAl_3(BO_3)_4$ [26]. These observations provide direct experimental evidence that the local structural environment of Er^{3+} can significantly modify its electronic states and may contribute to its anisotropic magnetic response.

$ErFe_3(BO_3)_4$ exhibits antiferromagnetic ordering at approximately 38–39 K, with significant contributions from Er^{3+} crystal-field effects and Er–Fe coupling [25,27]. Spectroscopic studies also show that the local Er^{3+} symmetry influences its electronic transitions and magnetic anisotropy [23,26]. These factors, together with magnetic

ordering, provide a physical context for investigating the magnetocaloric response of this compound [6–11,14,20,21].

Despite the extensive structural, spectroscopic, and magnetic investigations of $ErFe_3(BO_3)_4$ [13,22–27], its magnetocaloric response, particularly the magnetic entropy change and relative cooling power of polycrystalline samples, deserves further examination. Moreover, the relationship between the measured magnetocaloric parameters and the structural and magnetic characteristics reported for this compound has not been sufficiently clarified. In particular, the possible contributions of the local Er^{3+} environment, crystal-field effects, magnetic anisotropy, and Er^{3+}–Fe^{3+} coupling provide a relevant framework for interpreting its low-temperature magnetic entropy change.

In this work, we investigate the structural, magnetic, and magnetocaloric properties of polycrystalline $ErFe_3(BO_3)_4$. The magnetic entropy change and relative cooling power are evaluated from field-dependent magnetization measurements, and the results are discussed in relation to the crystallographic symmetry and the reported electronic and magnetic characteristics of the compound. The main contribution of this study is a combined analysis of the magnetic and magnetocaloric response, supported by a symmetry-informed interpretation of the possible roles of the local Er^{3+} environment and magnetic interactions. Since the present measurements do not directly determine the crystal-field levels or independently quantify the magnetic anisotropy, these mechanisms are discussed as possible contributions rather than as experimentally established causal relationships.

2. Experiment

2.1. Sample Preparation

High-purity Er_2O_3 (99.99%), Fe_2O_3 (99.99%), and H_3BO_3 (≥99.5%), all supplied by Sigma-Aldrich (St. Louis, MO, USA), were used as starting materials.

The precursors were weighed in accordance with the nominal stoichiometric composition of $ErFe_3(BO_3)_4$ and thoroughly homogenized in an agate mortar for approximately 30 min. The resulting mixture was transferred to an alumina crucible and calcined in air at 900 °C for 6 h, using a heating rate of approximately 3–5 °C min^{-1}.

After calcination, the material was allowed to cool naturally to room temperature and was thoroughly reground to ensure compositional homogeneity and promote the completion of the solid-state reaction. The resulting powder was then placed in an alumina crucible and sintered in air at 1200 °C for 4 h. Following sintering, the sample was naturally cooled to room temperature and finely ground to obtain a polycrystalline powder for subsequent structural, morphological, elemental, magnetic, and magnetocaloric characterization.

2.2. X-Ray Diffraction Analysis

Structural characterization was carried out using a Bruker D8 Advance diffractometer (Bruker AXS GmbH, Karlsruhe, Germany) with Cu Kα radiation (λ = 1.5406 Å). Diffraction patterns were recorded at room temperature over the 10–80° (2θ) range, with a step size of about 0.02°. Phase identification was performed by comparison with crystallographic reference data. Rietveld refinement was subsequently carried out using the FullProf Suite (2024), assuming the trigonal R32 space group (No. 155). The refined lattice parameters, unit-cell volume, and reliability factors were used to evaluate the agreement between the experimental data and the structural model. The refined structural parameters provided the crystallographic basis for discussing the structural characteristics of $ErFe_3(BO_3)_4$ in relation to its magnetic behavior.

2.3. Morphological and Chemical Characterization

The morphology of the synthesized powder was examined by scanning electron microscopy (SEM) using a ZEISS GeminiSEM 300 field-emission scanning electron microscope. The SEM observations were performed at an accelerating voltage of approximately 15 kV. The elemental composition was investigated by energy-dispersive X-ray spectroscopy (EDS/EDX) coupled to the SEM. The spectra were collected at several different locations on the sample to verify the homogeneous distribution of Er, Fe, and O and to check the absence of significant foreign elements. The EDS results were used to assess the local elemental composition; however, quantitative compositional homogeneity should only be claimed if supported by appropriate quantitative analyses or elemental maps.

2.4. Magnetic Measurements

Magnetic measurements of $ErFe_3(BO_3)_4$ were performed using a Quantum Design Physical Property Measurement System (PPMS) equipped with a vibrating sample magnetometer (VSM). The temperature dependence of magnetization, M(T), was measured in the temperature range of 7–250 K under an applied magnetic field of 5 mT (50 Oe). Additional measurements were performed under selected magnetic fields to investigate the magnetic behavior around the transition. Isothermal magnetization curves, M(H), were recorded at closely spaced temperatures around the magnetic ordering region and at lower temperatures, with the magnetic field varied from 0 to 7 T. The obtained magnetization data were used to calculate the magnetic entropy change associated with the applied field variation.

The measurements were performed on a polycrystalline $ErFe_3(BO_3)_4$ sample with a mass of approximately 48 mg. The sample was prepared as a pressed pellet with a diameter of 10 mm and a thickness of approximately 0.1 mm, without any binder. No demagnetizing-field correction was applied to the magnetization data. Given the relatively low magnetization values and the sample geometry, the demagnetizing effect was considered negligible within the experimental uncertainty. Accordingly, the internal magnetic field was approximated by the applied magnetic field in the present analysis.

3. Results and Discussion

Structural Analysis

$ErFe_3(BO_3)_4$ belongs to the rare-earth ferroborate family $ErFe_3(BO_3)_4$, The room-temperature crystal structure was analyzed using the trigonal R32 space group (No. 155) as the structural model for Rietveld refinement. As illustrated in Figure 1 the crystal structure consists of ErO_6 coordination polyhedra, FeO_6 octahedra, and BO_3 triangular groups. The Fe^{3+} ions are coordinated by oxygen atoms to form FeO_6 octahedra, which are connected through the borate groups and arranged in helicoidal chains along the crystallographic c-axis. The Er^{3+} ions occupy rare-earth sites coordinated by oxygen atoms. This local coordination environment provides a structural context for discussing the crystal-field effects and magnetic anisotropy of Er^{3+}.

The R32 space group is non-centrosymmetric and possesses a threefold crystallographic axis parallel to the c-axis. These symmetry characteristics are relevant to the local crystal-field environment and may contribute to the anisotropic magnetic behavior of $ErFe_3(BO_3)_4$. However, the specific influence of crystallographic symmetry on the magnetocaloric response cannot be established from the structural refinement alone.

Powder X-ray diffraction (XRD) measurements were performed at room temperature to investigate the crystal structure and phase purity of the synthesized $ErFe_3(BO_3)_4$ sample. Rietveld refinement (Figure 2) of the experimental diffraction pattern was carried out

using the FullProf Suite, adopting the trigonal R32 space group (No. 155) as the structural model. The refinement included the scale factor, background contribution, unit-cell parameters, peak-shape parameters, and structural parameters. The quality of the refinement was evaluated using the reliability factors Rp, Rwp, and Rexp, together with the goodness-of-fit parameter χ^2.

The refined crystallographic parameters are summarized in Table 1. The lattice parameters are a = b = 9.566 Å and c = 7.591 Å, corresponding to a unit-cell volume of 601.5 Å^3 and Z = 3 formula units per unit cell. The refinement yielded Rp = 5.21%, Rwp = 6.63%, Rexp = 3.44%, and χ^2 = 3.72, indicating reasonable agreement between the experimental and calculated diffraction patterns.

No significant additional reflections attributable to crystalline secondary phases were detected within the sensitivity of the XRD measurement. These results support the structural model adopted for the room-temperature diffraction data and provide the crystallographic basis for the subsequent discussion of the magnetic and magnetocaloric properties of $ErFe_3(BO_3)_4$.

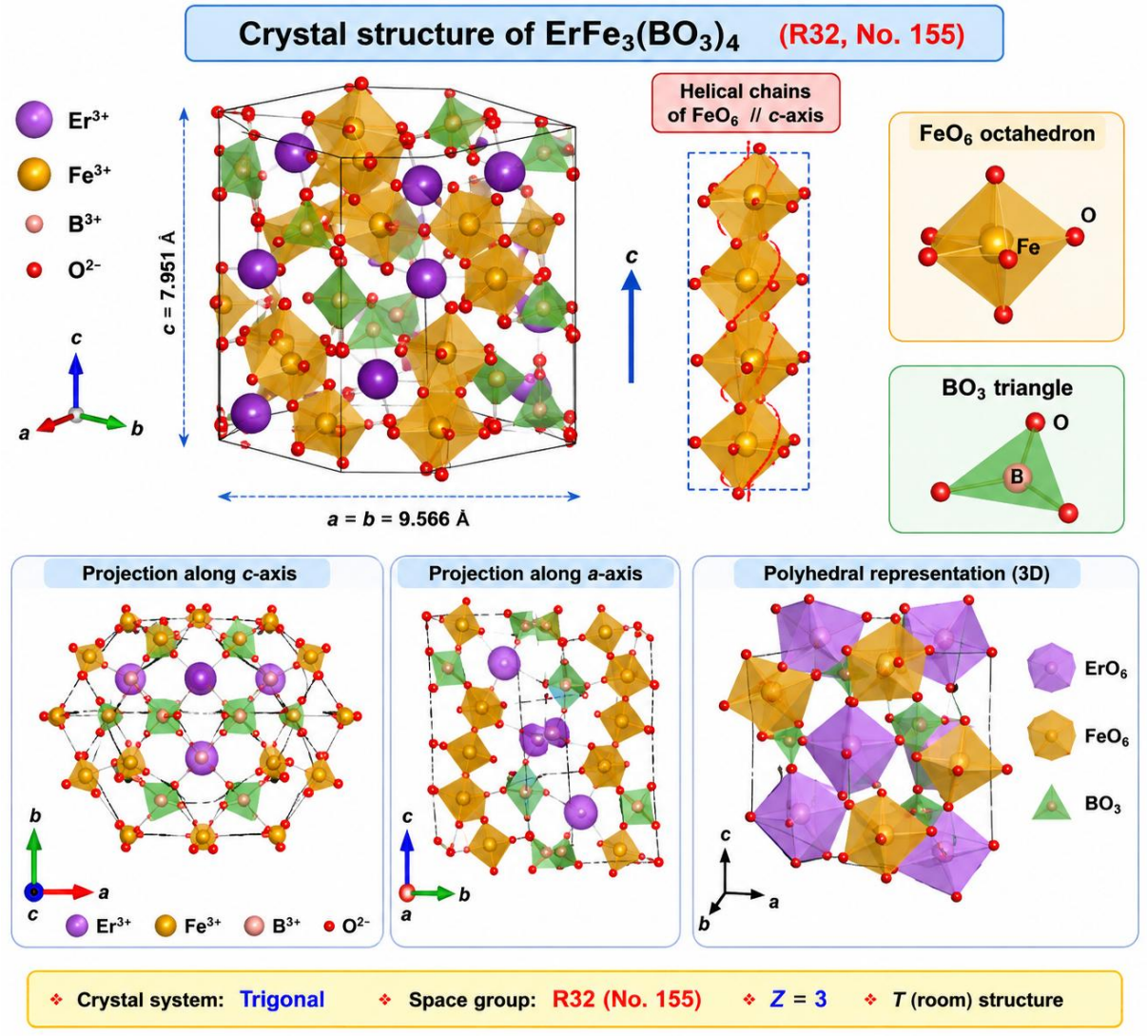


Figure 1. Crystal structure of trigonal $ErFe_3(BO_3)_4$ viewed along the principal crystallographic directions, showing the ErO_6 coordination units, FeO_6 octahedra, BO_3 groups, and the threefold c-axis associated with the R32 symmetry.

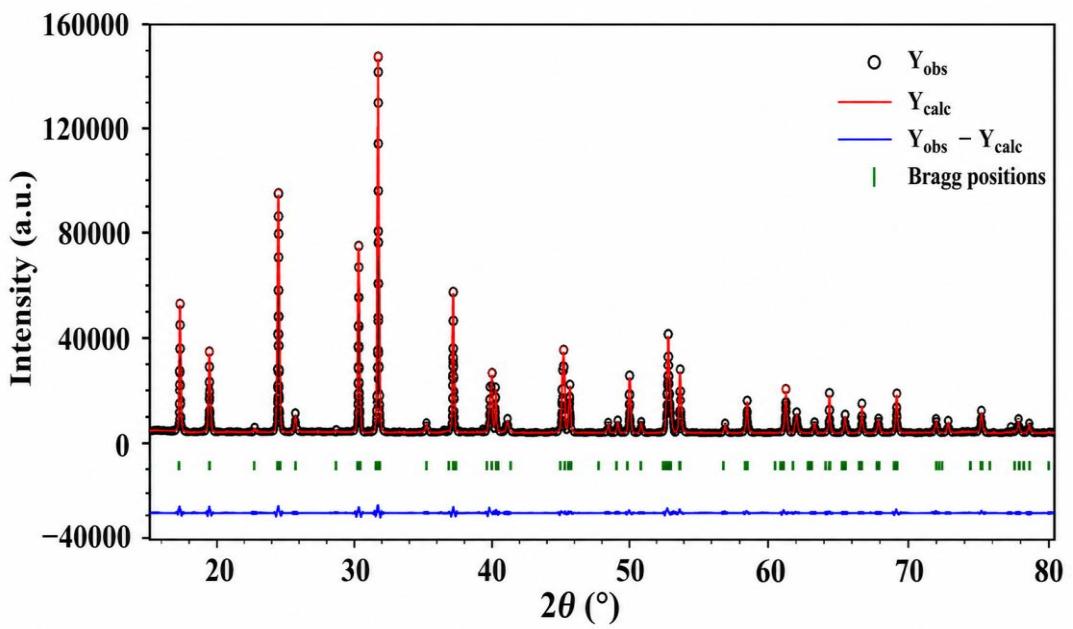


Figure 2. Rietveld refinement of the XRD pattern of $ErFe_3(BO_3)_4$. Experimental data, calculated profile, difference curve, and Bragg reflection positions corresponding to the trigonal R32 structure (No. 155) are shown.

Table 1. Crystallographic and Rietveld refinement parameters of $ErFe_3(BO_3)_4$.

Parameter	$ErFe_3(BO_3)_4$
Crystal system	Trigonal
Space group	R32 (No. 155)
a = b (Å)	9.566
c (Å)	7.591
V (Å^3)	601.5
Z	3
R_p (%)	5.21
R_{wp} (%)	6.63
R_{exp} (%)	3.44
χ^2	3.72

The surface morphology and elemental distribution of the synthesized $ErFe_3(BO_3)_4$ powder were investigated using scanning electron microscopy (SEM) coupled with energy-dispersive X-ray spectroscopy (EDS). The SEM images were examined to assess the particle morphology, particle-size distribution, agglomeration, and overall microstructural features.

As shown in Figure 3a, the SEM micrograph reveals irregularly shaped particles with a broad size distribution and noticeable agglomeration. Such agglomeration may be associated with the high-temperature thermal treatment during synthesis. The particles exhibit substantial interparticle contact, forming compact aggregates. No clearly distinguishable large morphological domains attributable to secondary phases are apparent in the investigated region. However, SEM morphology alone cannot establish phase purity.

The EDS elemental maps shown in Figure 3b–d illustrate the spatial distributions of Er, Fe, B, and O. The detected elemental signals appear broadly distributed across the analyzed region, with no obvious localized enrichment or depletion visible in the maps. This observation suggests a relatively uniform microscale distribution of the detected elements within the investigated area. Minor variations in signal intensity may arise from

surface topography, particle thickness, and differences in electron–matter interactions. Although the EDS maps provide qualitative evidence of the spatial distribution of the constituent elements, they do not by themselves establish exact stoichiometry or exclude minor compositional variations. Overall, the SEM and EDS results complement the XRD and Rietveld analyses by providing information on the powder morphology and the spatial distribution of its constituent elements.

The temperature-dependent magnetic response of $ErFe_3(BO_3)_4$, recorded under a low applied magnetic field of 5 mT, is presented in Figure 4. The M(T) curve reveals a clear magnetic anomaly in the vicinity of T_N = 38 K, consistent with the onset of antiferromagnetic ordering. Here, T_N denotes the Néel temperature, corresponding to the onset of antiferromagnetic ordering in $ErFe_3(BO_3)_4$. This behavior is consistent with the magnetic ordering reported previously for $ErFe_3(BO_3)_4$ [16,18]. The pronounced low-temperature response reflects the possible contributions of the Fe^{3+} magnetic sublattice and the Er^{3+} 4f moments.

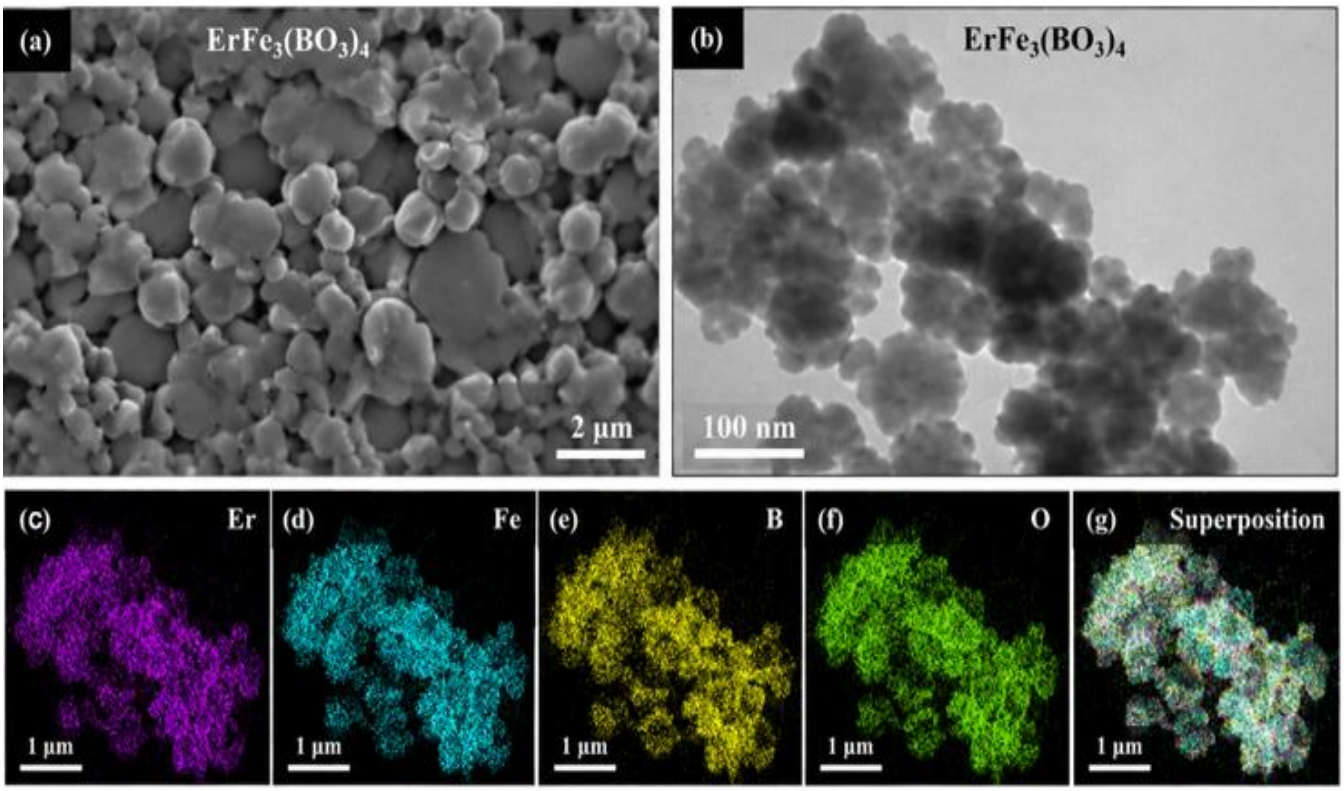


Figure 3. (**a**) SEM micrograph of $ErFe_3(BO_3)_4$; (**b**) TEM image; (**c**–**f**) EDS elemental mapping showing the spatial distribution of Er, Fe, B, and O; (**g**) EDS spectrum confirming the presence of the constituent elements.

From a symmetry perspective, this magnetic behavior can be discussed in relation to the crystallographic environment of the rare-earth ion. Previous studies have reported the lower-symmetry P3121 structure for $ErFe_3(BO_3)_4$ over a broad temperature range, although the associated structural distortion may be difficult to resolve by conventional X-ray diffraction [17]. This lower local symmetry may influence the crystal-field splitting of the Er^{3+} 4f states and the associated magnetic anisotropy. Owing to the strong spin–orbit coupling of Er^{3+}, its magnetic response can be sensitive to changes in the local crystal-field environment.

The magnetic ordering is primarily associated with interactions within the Fe^{3+} sublattice, while the Er^{3+} crystal-field states and the exchange coupling between Er^{3+} and Fe^{3+} may contribute to the low-temperature magnetic response. These microscopic

mechanisms provide a plausible framework for interpreting the measured magnetization, but their individual contributions cannot be established from the M(T) curve alone. The low-temperature magnetic response may reflect the interplay between Fe^{3+}–Fe^{3+} exchange interactions, the crystal-field effects associated with Er^{3+}, and the exchange coupling between the Fe^{3+} and Er^{3+} sublattices.

Overall, the M(T) results establish the characteristic magnetic ordering temperature of $ErFe_3(BO_3)_4$ and provide a basis for analyzing its magnetocaloric properties using the isothermal magnetization curves, M(H). The possible influence of the local Er^{3+} environment and magnetic anisotropy on the magnetocaloric response is considered in the following section.

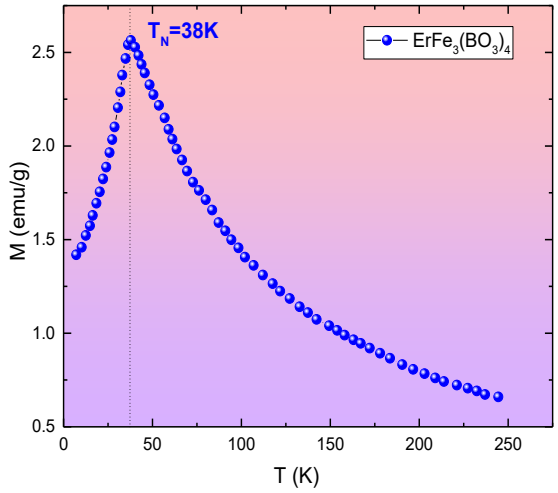


Figure 4. Magnetization versus temperature for $ErFe_3(BO_3)_4$ at an applied field of 50 Oe (5 mT).

The isothermal magnetization curves, M(H), of $ErFe_3(BO_3)_4$ measured at selected temperatures around the magnetic ordering region are presented in Figure 5. The magnetization increases progressively with the applied magnetic field, while its magnitude exhibits a pronounced temperature dependence near T_n. This behavior reflects the field-dependent response of the magnetic system in the vicinity of the ordering transition and provides the experimental basis for evaluating its magnetocaloric properties. In particular, no abrupt magnetization jump or pronounced hysteresis is observed in the measured M(H) curves, indicating the absence of clear signatures of a first-order field-induced magnetic transition.

The observed magnetic response can be interpreted in terms of the contributions of the Fe^{3+} and Er^{3+} sublattices. The magnetic behavior is primarily associated with interactions within the Fe^{3+} sublattice, while the crystal-field effects acting on the Er^{3+} 4f states, together with the exchange coupling between the Fe^{3+} and Er^{3+} moments, may also influence the field-dependent magnetization. Owing to the strong spin–orbit coupling of Er^{3+}, its magnetic response can be sensitive to the local crystal-field environment and the resulting magnetic anisotropy. The crystallographic environment of Er^{3+}, together with spin–orbit coupling and exchange interactions between the Fe^{3+} and Er^{3+} sublattices, may contribute to the magnetic-field dependence of the magnetization.

The temperature dependence of the isothermal curves is particularly evident near T_n, where the magnetic response changes as the system approaches the ordering transition. This behavior is relevant to the magnetocaloric effect because the field-induced variation in magnetization is used to calculate the magnetic entropy change. This feature is potentially favorable for magnetocaloric applications, although a complete assessment of

reversibility also requires consideration of the associated entropy change and any field-cycling losses.

The nature of the magnetic transition in $ErFe_3(BO_3)_4$ was further investigated using Arrott plots, constructed by plotting M^2 as a function of μ_0H/M from the isothermal magnetization data, as shown in Figure 6. This analysis provides a macroscopic criterion for assessing the order of the magnetic transition.

The high-field regions of the Arrott plots exhibit predominantly positive slopes, with no evident negative-slope regions. According to the Banerjee criterion, this behavior is consistent with a second-order magnetic transition. The continuous evolution of the Arrott curves across the investigated temperature range is also consistent with the magnetic anomaly observed in the M(T) measurements near $T_N \approx 38$ K, supporting the interpretation of a continuous magnetic transition.

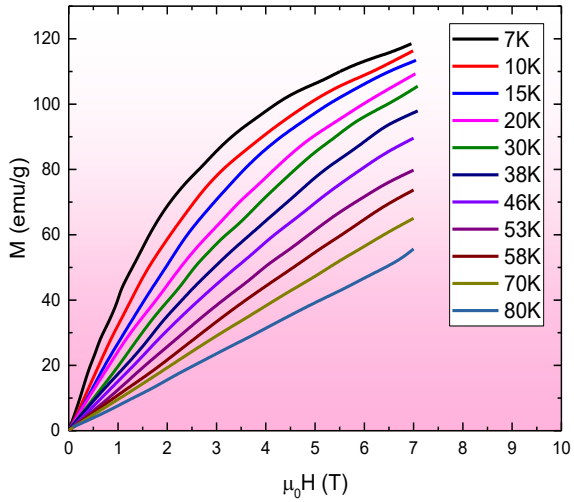


Figure 5. Isothermal magnetization M(H) curves of $ErFe_3(BO_3)_4$ around the magnetic ordering temperature.

The magnetic behavior can be discussed in the context of the crystallographic environment and the interactions between the Fe^{3+} and Er^{3+} sublattices. The local crystal-field environment of Er^{3+}, together with spin–orbit coupling and exchange interactions, may influence the magnetic anisotropy and field-dependent response. These factors provide a physical context for interpreting the magnetization behavior, although their individual contributions cannot be determined from the Arrott plots alone.

The transition order is relevant to the magnetocaloric properties of $ErFe_3(BO_3)_4$ because the magnetic entropy change is evaluated from the field and temperature dependence of the magnetization. A predominantly second-order transition is generally associated with a continuous magnetic response and may favor a reversible magnetocaloric effect over a broad temperature interval. Accordingly, the Arrott analysis complements the magnetization measurements and supports the interpretation of the magnetic transition underlying the observed magnetocaloric response.

The calculation of the MCE was performed by evaluating the isothermal magnetic entropy change ($-\Delta S_M$) from isothermal magnetization measurements using the Maxwell equation:

$$\Delta S_M(T, \Delta H) = \int_0^{\mu_0 H_{max}} \left(\frac{\partial M}{\partial T}\right)_H d(\mu_0 H) \quad (1)$$

For the discrete experimental M(H) data, the entropy change was numerically evaluated from successive isothermal magnetization curves.

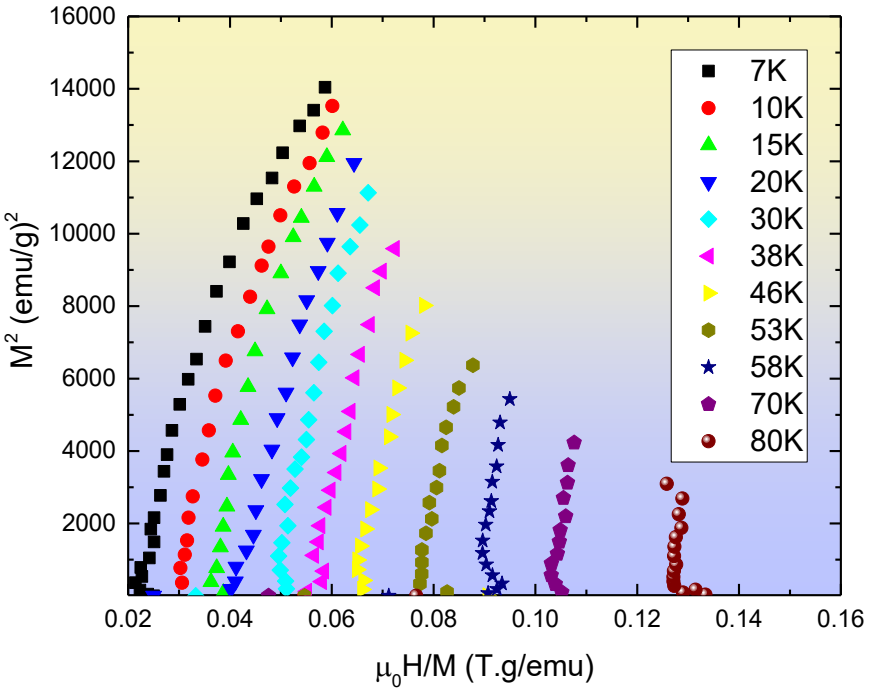


Figure 6. Arrott plots (M^2 versus $\mu_0 H/M$) of $ErFe_3(BO_3)_4$ around the magnetic transition.

The resulting $-\Delta S_M$ (T) profiles for different magnetic-field changes are presented in Figure 7. For a field change of 0–7 T, the maximum magnetic entropy change reaches approximately

$$-\Delta S_{M\ max} \approx 9.0\ J\ kg^{-1}\ K^{-1}.$$

The maximum occurs near the low-temperature magnetic ordering region, reflecting field-induced changes in the magnetic configuration of the Fe^{3+} and Er^{3+} sublattices.

The observed maximum in $-\Delta S_M$ near the magnetic ordering region is therefore consistent with the strong temperature dependence of magnetization identified from the M(T) and M(H) measurements. Near T_N, relatively small changes in temperature can produce substantial changes in the magnetic configuration, resulting in a large value of $(\partial M/\partial T)_H$ and, consequently, an enhanced magnetic entropy change.

To further assess the practical refrigeration performance of $ErFe_3(BO_3)_4$, the temperature-averaged entropy change (TEC) and relative cooling power (RCP) were subsequently evaluated and are presented in Figure 8. The TEC was calculated according to:

$$\mathrm{TEC}\ (\Delta T_{lift}) = \max_{T_{mid}} \left[\frac{1}{\Delta T_{lift}} \int_{T_{mid}-\Delta T_{lift}/2}^{T_{mid}+\Delta T_{lift}/2} -\Delta S_M(T)\ dT \right] \quad (2)$$

where ΔT_{lift} is the operating temperature span and Tmid is the central temperature of the selected operating interval. In the present work, ΔT_{lift} = 5 K was selected to evaluate the refrigeration performance of $ErFe_3(BO_3)_4$.

Under 0–7 T, the maximum magnetic entropy change reaches approximately 9.0 J kg^{-1} K^{-1}, whereas the entropy change averaged over the selected 5 K temperature span reaches approximately 8.20 J kg^{-1} K^{-1}. The relatively small difference between $(-\Delta S_M)^{max}$ and TEC(5K) indicates that the magnetic entropy change remains relatively high over the selected temperature interval.

https://doi.org/10.3390/magnetochemistry12110129

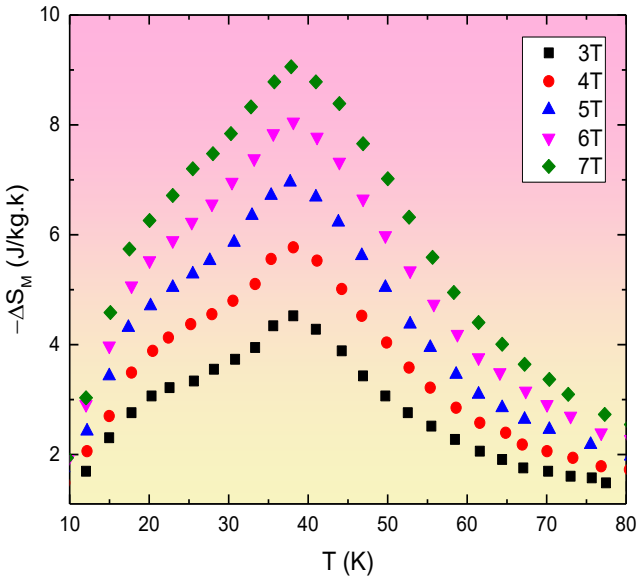


Figure 7. Magnetic entropy change ($-\Delta S_m$) of $ErFe_3(BO_3)_4$ as a function of temperature for different magnetic-field changes, highlighting the maximum magnetocaloric response near the magnetic ordering temperature.

The relative cooling power (RCP) was evaluated to further characterize the magnetocaloric response of $ErFe_3(BO_3)_4$. The RCP was determined from the maximum magnetic entropy change, $-\Delta S_M^{max}$ and the corresponding full width at half maximum, δT_{FWHM}, according to:

$$RCP = (-\Delta S_M^{max}) \times \delta T_{FWHM} \quad (3)$$

The temperature dependence of the magnetocaloric parameters, including the RCP and TEC, is presented in Figure 8. The TEC averaged over a 5 K temperature interval, TEC(5 K), is approximately 8.20 J kg^{-1} K^{-1}, while the maximum magnetic entropy change, $-\Delta S_M^{max}$, and the RCP reach approximately 9.0 J kg^{-1} K^{-1} and 235 J kg^{-1}, respectively, under a magnetic-field change of 0–7 T. The TEC complements the maximum magnetic entropy change and RCP by quantifying the average entropy change over a defined operating temperature interval.

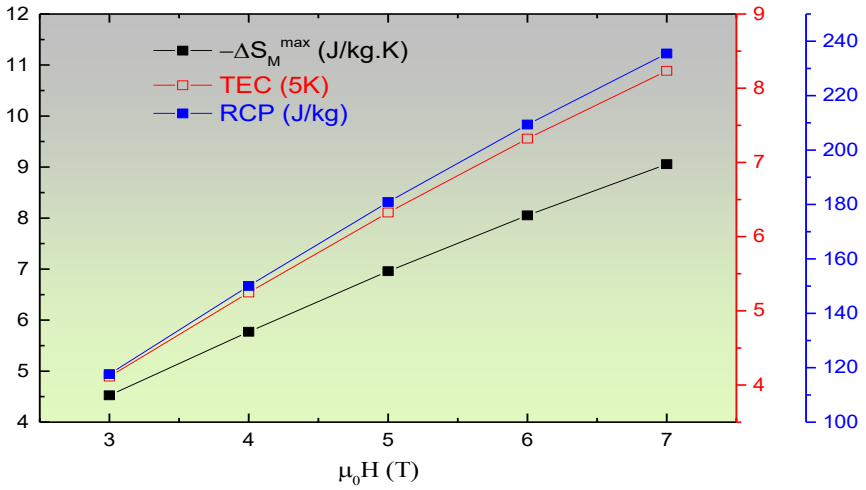


Figure 8. Magnetic entropy change ($-\Delta S_m$), temperature-averaged entropy change TEC (5 K), and relative cooling power (RCP) of $ErFe_3(BO_3)_4$ as a function of magnetic-field change.

https://doi.org/10.3390/magnetochemistry12110129

The magnetocaloric response of $ErFe_3(BO_3)_4$ can be considered in the broader context of rare-earth-containing magnetic compounds, for which the magnetic entropy change is governed by the interplay between the magnetic ground state, exchange interactions, crystal-field effects, magnetic anisotropy, applied magnetic field, and temperature.

Under a field change of 0–7 T, $ErFe_3(BO_3)_4$ reaches a maximum magnetic entropy change of about 9.0 J kg^{-1} K^{-1} and an RCP of roughly 235 J kg^{-1}. Other rare-earth borates studied recently exhibit a wide range of magnetocaloric responses, reflecting differences in their magnetic and structural properties. Gd_3TeBO_9, for instance, reaches 57.44 J kg^{-1} K^{-1} at 2.6 K under 7 T [28], while $Eu_2B_2O_5$ gives maximum entropy changes of 13.7, 28.2, and 46.9 J kg^{-1} K^{-1} for field changes of 0–1, 0–2, and 0–5 T, respectively [29]. $Ba_5Gd_3(BO_3)_6F$ has been reported to reach a maximum $-\Delta S_m$ of 29.86 J kg^{-1} K^{-1} at 3 K under 9 T [30]. Similarly, $Sr_{14.06}Gd_{14.63}(BO_3)_{24}$ exhibits a maximum magnetic entropy change of 42.2 J kg^{-1} K^{-1} at 2 K under 7 T [33]. More recently, $LiCaGd_5(BO_3)_6$ was reported to exhibit a large $-\Delta S_m$ value of 40.8 J kg^{-1} K^{-1} under a relatively low field change of 0–2 T [34]. $KBaGd(BO_3)_2$ also exhibits a substantial cryogenic magnetocaloric response, with a maximum entropy change of 15.47 J mol^{-1} K^{-1} at 2 K under 7 T, corresponding to approximately 34.3 J kg^{-1} K^{-1} [35]. These differences may be associated with variations in the rare-earth ions, magnetic concentrations, exchange interactions, ordering temperatures, crystal-field schemes, and crystallographic environments of the investigated compounds.

The influence of magnetic anisotropy provides an additional framework for understanding this behavior. Recent investigations of anisotropic rare-earth compounds, such as $DyTe_3$ and NdGaSi, have demonstrated that the magnetocaloric response depends strongly on the crystallographic direction and the associated magnetic anisotropy [31,32]. In $DyTe_3$, a maximum $-\Delta S_M$ of 14.75 J kg^{-1} K^{-1} was obtained under 7 T along the easy plane, accompanied by a significant anisotropic magnetocaloric response [31]. Similarly, NdGaSi exhibits a pronounced anisotropic and rotating magnetocaloric effect, with a rotating entropy change of 20.6 J kg^{-1} K^{-1} under 5 T [32]. Overall, these comparisons place the magnetocaloric response of $ErFe_3(BO_3)_4$ within the broader range of behaviors reported for rare-earth-based magnetic materials. Its maximum entropy change and RCP provide useful quantitative measures of its performance under a field change of 0–7 T, while further investigation of the magnetic anisotropy and the respective contributions of the Fe^{3+} and Er^{3+} sublattices would help clarify the microscopic factors governing its response.

4. Conclusions

The magnetic and magnetocaloric properties of $ErFe_3(BO_3)_4$ were systematically investigated within a symmetry-based framework. The structural analysis confirms the formation of the targeted trigonal ferroborate phase, while the SEM–EDS characterization reveals a relatively homogeneous microstructure and a uniform spatial distribution of the constituent elements. The temperature-dependent magnetization identifies a clear magnetic ordering transition at approximately $T_N \approx 38$ K, establishing the characteristic temperature scale governing the magnetic response of the compound.

The isothermal magnetization behavior further demonstrates a pronounced field and temperature dependence around the ordering region, without significant hysteresis over the investigated field range. Arrott analysis, based on the Banerjee criterion, indicates a second-order character of the magnetic transition. This continuous magnetic behavior provides an appropriate thermodynamic framework for the observed field-induced entropy variation.

The magnetocaloric analysis reveals a pronounced magnetic entropy change, reaching approximately $\mathbf{(-\Delta S_M)^{max}} \approx 9.0$ J kg^{-1} K^{-1} under a magnetic-field change of 0–7 T. The response is concentrated around the magnetic ordering region, reflecting the strong temperature dependence of the magnetization near T_N. Furthermore, the temperature-

averaged entropy change, TEC(5 K) ≈ 8.20 J kg^{-1} K^{-1}, and the relative cooling power, RCP ≈ 235 J kg^{-1}, characterize the magnitude and temperature distribution of the magnetocaloric response over a finite temperature interval.

The magnetic response can be discussed in terms of the interplay between the Fe^{3+} and Er^{3+} magnetic sublattices, crystal-field effects, spin–orbit coupling, and exchange interactions. The local environment of Er^{3+} may contribute to the magnetic anisotropy and field-dependent response; however, the individual contributions of these factors to the measured magnetocaloric effect require further investigation.

Overall, the results demonstrate that the magnetocaloric behavior of $ErFe_3(BO_3)_4$ is characterized by the interplay between its magnetic ordering, field-dependent magnetization, and crystallographic environment. The combined structural, magnetic, and magnetocaloric analyses provide a coherent description of the material's behavior and establish its magnetocaloric parameters under a field change of 0–7 T. These findings provide a basis for further investigations of the relationship between local crystal-field effects, magnetic interactions, and magnetocaloric performance in rare-earth ferroborates.

Author Contributions: Investigation, A.E., P.G. and Z.F.; methodology, A.E., P.G. and Z.F.; software, A.E. and P.G.; validation, A.E., P.G., Z.F., M.N.K., A.A.A. and C.J.R.; writing—original draft preparation, A.E. and Z.F.; writing—review and editing, P.G. and C.J.R.; resources, M.N.K. and A.A.A.; supervision, M.N.K., A.A.A. and C.J.R.; project administration, M.N.K., A.A.A. and C.J.R.; data curation, C.J.R. All authors have read and agreed to the published version of the manuscript.

Funding: This research was supported by the National Research Foundation of Korea (NRF) grant funded by the Korea government (MSIT) (RS-2026-25596351).

Institutional Review Board Statement: Not applicable.

Informed Consent Statement: Not applicable.

Data Availability Statement: The original contributions presented in this study are included in the article. Further inquiries can be directed to the corresponding authors.

Acknowledgments: The authors extend their appreciation to the Deanship of Scientific Research, Islamic University of Madinah, Saudi Arabia, for funding this research work.

Conflicts of Interest: The authors declare no conflicts of interest.

References

1. Pankratov, N.Y.; Tereshina, I.S.; Nikitin, S.A. Magnetocaloric effect in Rare-Earth magnetic materials. *Phys. Met. Metallogr.* **2023**, *124*, 1093–1101. https://doi.org/10.31857/s0015323023601095.
2. Elouafi, A.; Derkaoui, S.; Moubah, R.; Tizliouine, A.; Charkaoui, A.; Lassri, H. Large magnetocaloric effect in Er_2O_3 compounds at cryogenic temperature. *J. Rare Earths* **2021**, *39*, 1232–1237. https://doi.org/10.1016/j.jre.2020.09.020.
3. Xu, J.; Zheng, X.; Xi, L.; Kan, X.; Bao, B.; Ma, T.; Zang, Y.; Wang, D.; Wang, D.; Gao, Y.; et al. Significant enhancement of magnetocaloric effects via tuning Curie temperature and magnetic anisotropy in rare-earth based compounds. *Appl. Mater. Today* **2023**, *35*, 101982. https://doi.org/10.1016/j.apmt.2023.101982.
4. Elouafi, A.; Fadil, Z.; Jabar, A.; Khan, M.N.; Alsayyari, A.A.; Raorane, C.J. Experimental Study on the Interplay Between Electrical Transport, Magnetism, Magnetocaloric and Magnetoresistive Effects in $Pr_{0.75}La_{0.05}K_{0.2}MnO_3$ Perovskite. *Ceram. Int.* **2026**, *52*, 27219–27228.
5. Neupane, D.; Kramer, N.; Bhattarai, R.; Hanley, C.; Pathak, A.K.; Shen, X.; Karna, S.; Mishra, S.R. Rare-Earth Doped $GD_{3-x}RE_xFE_5O_{12}$ (RE = Y, ND, SM, and DY) Garnet: Structural, Magnetic, Magnetocaloric, and DFT study. *Ceramics* **2023**, *6*, 1937–1976. https://doi.org/10.3390/ceramics6040120.
6. Elouafi, A.; Lmai, F.; Tizliouine, A.; El-bachiri, A.; Chafi, M.; Fadil, Z.; Raorane, C.J. Structural, magnetic and large magnetocaloric effect in terbium orthophosphate $TbPO_4$ near superfluid helium. *J. Solid State Chem.* **2026**, *360*, 126079. https://doi.org/10.1016/j.jssc.2026.126079.

7. Shin, H.J.; Kim, J.S.; Jeong, K.W.; Kim, J.H.; Lee, N.; Choi, Y.J. Giant and highly anisotropic magnetocaloric effects in single crystals of disordered-perovskite $RCr_{0.5}Fe_{0.5}O_3$ (R = Gd, Er). *Sci. Rep.* **2023**, *13*, 7105. https://doi.org/10.1038/s41598-023-34258-w.
8. Cho, K.; Shon, W.; Bae, J.; Lee, J.; Yoon, S.; Kim, J.; Rhyee, J.; Cho, B. Anisotropic metamagnetic spin reorientation and rotational magnetocaloric effect of single crystal NDALGE. *Materials* **2023**, *16*, 2771. https://doi.org/10.3390/ma16072771.
9. Damay, F.; Petit, S.; Sheptyakov, D.; Colin, C.V.; Suard, E.; Rols, S.; Embs, J.; Stuhr, U.; Bounoua, D.; Demortier, O.; et al. Influence of Dy^{3+} environment on magnetic anisotropy and magnetocaloric effect in $Dy_3B_2C_3O_{12}$ (B=In,Sc,Te;C=Ga,Al,Li) garnets. *Phys. Rev. B* **2024**, *109*, 014419. https://doi.org/10.1103/PhysRevB.109.014419.
10. Kanda, T.; Ishikawa, H.; Imajo, S.; Kindo, K.; Tanida, H.; Kohama, Y. Magnetic anisotropy of CeCoSi under high magnetic field. *Phys. Rev. B* **2024**, *109*, 174402. https://doi.org/10.1103/physrevb.109.174402.
11. Hayami, S. Symmetry Classification of Antiferromagnets with Four Types of Multipoles. *Symmetry* **2024**, *16*, 926. https://doi.org/10.3390/sym16070926.
12. Liu, Y.; Chen, X.; Yu, Y.; Etxebarria, J.; Perez-Mato, J.M.; Liu, Q. Symmetry classification of magnetic orders using oriented spin space groups. *Nature* **2026**, *652*, 869–873. https://doi.org/10.1038/s41586-026-10401-1.
13. Alekseeva, O.; Smirnova, E.; Frolov, K.; Lyubutina, M.; Lyubutin, I.; Gudim, I. Crystal structure dynamics of $RFE_3(BO_3)_4$ single crystals in the temperature range 25–500 k. *Crystals* **2022**, *12*, 1203. https://doi.org/10.3390/cryst12091203.
14. Tacconi, L.; Manvell, A.S.; Briganti, M.; Czernia, D.; Weihe, H.; Konieczny, P.; Bendix, J.; Perfetti, M. Exploiting high order magnetic anisotropy for advanced magnetocaloric refrigerants. *Angew. Chem. Int. Ed.* **2024**, *64*, e202417582. https://doi.org/10.1002/anie.202417582.
15. Ritter, C.; Vorotynov, A.; Pankrats, A.; Petrakovskii, G.; Temerov, V.; Gudim, I.; Szymczak, R. Magnetic structure in iron borates $RFe_3(BO_3)_4$ (R = Er, Pr): A neutron diffraction and magnetization study. *J. Phys. Condens. Matter* **2010**, *22*, 206002. https://doi.org/10.1088/0953-8984/22/20/206002.
16. Ritter, C.; Vorotynov, A.; Pankrats, A.; Petrakovskii, G.; Temerov, V.; Gudim, I.; Szymczak, R. Magnetic structure in iron borates $RFe_3(BO_3)_4$ (R = Y, Ho): A neutron diffraction and magnetization study. *J. Phys. Condens. Matter* **2008**, *20*, 365209. https://doi.org/10.1088/0953-8984/20/36/365209.
17. Ritter, C.; Pankrats, A.; Gudim, I.; Vorotynov, A. Determination of the magnetic structure of $SmFe_3(BO_3)_4$ by neutron diffraction: Comparison with other $RFe_3(BO_3)_4$ iron borates. *J. Phys. Condens. Matter* **2012**, *24*, 386002. https://doi.org/10.1088/0953-8984/24/38/386002.
18. Demidov, A.A.; Kolmakova, N.P.; Takunov, L.V.; Volkov, D.V. Magnetoelastic effects in the trigonal 4f–3d crystals: $RFe_3(BO_3)_4$. *Phys. B Condens. Matter* **2007**, *398*, 78–84. https://doi.org/10.1016/j.physb.2007.04.075.
19. Jena, M.; Alam, M.; Dani, S.; Ghosh, S.; Fatema, M.; Lamba, M.; Bandyopadhyay, K.; Saha, S.; Mukherjee, S.; Iyer, K.K.; et al. Anisotropic magnetocaloric effect and spin-phonon coupling in two-dimensional van der Waals $FePS_3$. *Phys. Rev. B* **2026**, *113*, 064429. https://doi.org/10.1103/z52p-twzm.
20. Balli, M.; Jmal, S.A.; Chdil, O.; Mansouri, S.; Fournier, P.; Jandl, S.; Salvestrini, J. Magnetic and magnetocaloric properties of $YBVO_3$ single crystals: Experiments and DFT calculations. *ACS Appl. Energy Mater.* **2025**, *8*, 12415–12427. https://doi.org/10.1021/acsaem.5c02110.
21. Gao, Y.; Zheng, X.; Wu, H.; Xu, J.; Huang, H.; Wang, D.; Liu, H.; Zhen, S.; Pan, Y.; Xi, L.; et al. Insight into the spin reorientation phase transition in the magnetocaloric NDNI compound. *Adv. Electron. Mater.* **2025**, *11*, 2500119. https://doi.org/10.1002/aelm.202500119.
22. Gu, Y.; Yang, F.; Won, C.; Cheong, S.; Birol, T.; Musfeldt, J.L. Pressure triggers structural phase transitions in Chiral $ERFE_3(BO_3)_4$. *J. Phys. Chem. C* **2026**, *130*, 1248–1256. https://doi.org/10.1021/acs.jpcc.5c07666.
23. Zhang, S.; Wang, Y.; Su, K.; Wang, H.; Yang, L.; Huang, S. Large magnetoresistance and magnetocaloric effects in a magnetostrictive $DyMn_2Ge_2$ single crystal. *Phys. Rev. B* **2026**, *113*, 054431. https://doi.org/10.1103/n3p9-cm7r.
24. Bae, J.; Han, S.; Cho, B. Cryogenic magnetocaloric performance in single-crystalline $Er_{1-x}Tm_xAl_2$ (x=0, 0.1, and 0.3). *J. Alloys Compd.* **2026**, *1065*, 187729. https://doi.org/10.1016/j.jallcom.2026.187729.
25. Popova, E.; Chukalina, E.; Boldyrev, K.; Jablunovskis, A.; Gudim, I. Magnetic structure of $ErFe_3(BO_3)_4$: Spectroscopic and thermodynamic studies. *J. Magn. Magn. Mater.* **2019**, *500*, 166374. https://doi.org/10.1016/j.jmmm.2019.166374.
26. Malakhovskii, A.; Sokolov, V.; Gudim, I. Influence of the low local symmetry of Er3+ ions on magnetic circular dichroism and absorption spectra of f-f transitions in $ErFe_3(BO_3)_4$ single crystal. *J. Magn. Magn. Mater.* **2018**, *465*, 700–708. https://doi.org/10.1016/j.jmmm.2018.06.057.

27. opova, E.A.; Vasiliev, A.N.; Temerov, V.L.; Bezmaternykh, L.N.; Tristan, N.; Klingeler, R.; Büchner, B. Magnetic and specific heat properties of $YFe_3(BO_3)_4$ and $ErFe_3(BO_3)_4$. *J. Phys. Condens. Matter* **2010**, *22*, 116006. https://doi.org/10.1088/0953-8984/22/11/116006.
28. Zhou, C.; Li, R. Gd_3TeBO_9: A Rare-Earth Borate with Significant Magnetocaloric Effect. *Chem.—A Eur. J.* **2023**, *30*, e202303048. https://doi.org/10.1002/chem.202303048.
29. Mo, Z.; Liu, Q.; Hao, W.; Li, L.; Xie, H.; Fu, Q.; Gao, X.; Shen, J. Magnetic properties and large low-field cryogenic magnetocaloric effect in the divalent europium borate $Eu_2B_2O_5$ compound. *Mater. Today Phys.* **2024**, *41*, 101351. https://doi.org/10.1016/j.mtphys.2024.101351.
30. Chen, Y.; Gong, P.; Chen, Z.; Liu, J.; Guo, R.; Shen, J.; Tu, H.; Zhang, G. $Ba_5Gd_3(BO_3)_6F$: A new alkaline earth-rare earth fluoroborate with magnetocaloric effect. *J. Solid State Chem.* **2024**, *335*, 124727. https://doi.org/10.1016/j.jssc.2024.124727.
31. Xia, Z.; Jiang, L.; Chen, H.; Hu, C.; Hu, C.; Tang, F.; Fang, Y.; Hu, J.; Han, Z. Anisotropic magnetocaloric effect in antiferromagnetic $DyTe_3$ single crystal. *Solid State Commun.* **2025**, *404*, 116119. https://doi.org/10.1016/j.ssc.2025.116119.
32. Zhong, R.; Yu, Z.; Luo, X.; Chen, C.; Lv, B.; Luo, Q.; Yang, H.; Gao, F.; You, H.; He, W.; et al. Large anisotropic magnetocaloric effect in Weyl-semimetal candidate NdGaSi single crystal. *J. Magn. Magn. Mater.* **2025**, *617*, 172855. https://doi.org/10.1016/j.jmmm.2025.172855.
33. Chen, Y.; Liu, W.; Wang, D.; Wang, N.; Fan, F.; Shen, J.; Zhang, G.; Song, H.; Tu, H. $Sr_{14.06}Gd_{14.63}(BO_3)_{24}$: A Gadolinium-Rich Borate with Magnetic Refrigeration Performance. *Inorg. Chem.* **2023**, *62*, 10263–10268. https://doi.org/10.1021/acs.inorgchem.3c01060.
34. Zhang, Z.; Sun, G.; Jiang, K.; Zhang, Z.; Li, L. A Geometrically Frustrated $LiCaGd_5(BO_3)_6$ Oxide with a Record Low-Field Magnetocaloric Response at Ultra-Low Temperature. *Adv. Funct. Mater.* **2026**, *36*, e76221. https://doi.org/10.1002/adfm.76221.
35. Xiong, Z.; Hussain, G.; Shanta, B.; Zhou, X.; Zhang, N.; Huang, D.; Huang, X.; Zheng, C.; Yue, Y.; Wang, X. Low-Temperature Magnetocaloric Behavior of $KBaRE(BO_3)_2$ (RE = Gd, Tb): Raman Spectroscopic Insights. *J. Alloys Compd.* **2026**, *1072*, 188829. https://doi.org/10.1016/j.jallcom.2026.188829.

Disclaimer/Publisher's Note: The statements, opinions and data contained in all publications are solely those of the individual author(s) and contributor(s) and not of MDPI and/or the editor(s). MDPI and/or the editor(s) disclaim responsibility for any injury to people or property resulting from any ideas, methods, instructions or products referred to in the content.